Sustainable Energy & Fuels

ROYAL SOCIETY OF CHEMISTRY

PAPER

View Article Online
View Journal | View Issue

Cite this: *Sustainable Energy Fuels*, 2022, **6**, 5491

Well-defined hierarchical teddy bear sunflower-like $NiCo_2O_4$ electrocatalyst for superior water oxidation†

Pradnya M. Bodhankar, [ab] Dattatray S. Dhawale, *[c] Sarbjit Giddey,[c] Ravi Kumar[de] and Pradip B. Sarawade*[ab]

The development of a robust and efficient electrocatalyst for water oxidation is challenging due to the large overpotential requirement to transfer four electrons. Herein, a novel spinel-type hierarchical teddy bear sunflower-like $NiCo_2O_4$ electrocatalyst was synthesized through the facile solvothermal process and evaluated for the challenging and demanding oxygen evolution reaction (OER) in the water electrolysis process. The teddy bear sunflower-like $NiCo_2O_4$ supported on nickel foam (NF) delivers a current density of 50 mA cm^{-2} at a small water oxidation overpotential (η_{50} = 319 mV) which is significantly lower than that of the corresponding spherical NiO/NF (η_{50} = 338 mV), and sea-urchin like Co_3O_4/NF (η_{50} = 357 mV). A large specific and electroactive surface area, as well as a high TOF value exhibited by the hierarchical teddy bear sunflower-like $NiCo_2O_4$ electrocatalyst, demonstrates the potential of $NiCo_2O_4$ to catalyze the water oxidation reaction efficiently. The impact of the near-Fermi-level d-orbital states in $NiCo_2O_4$ electrocatalyst for boosting OER activity was unveiled by the density functional theory calculation. The stable performance even after 16 h and high catalyst utilization of the hierarchical teddy bear sunflower-like $NiCo_2O_4$ through the OER indicates that the catalyst is highly suitable for the large-scale water oxidation process.

Received 13th August 2022
Accepted 3rd November 2022

DOI: 10.1039/d2se01111e

rsc.li/sustainable-energy

1. Introduction

At present, hydrogen generation *via* water splitting has been the subject of research for the reason that green energy plays a crucial role in environmental fortification.[1] The hydrogen evolution reaction (HER) and oxygen evolution reaction (OER) occur at the cathode and anode, respectively and are the processes involved in electrochemical water-splitting. In this mechanism, the OER is of particular interest, as it is a four-electron transport reaction and demands high overpotential.[2,3] In this context, it is imperative to develop highly efficient and stable water oxidation electrocatalysts that will reduce the overpotential value and accelerate the process. To date, noble metal-based catalysts such as the oxides of ruthenium (RuO_2) and iridium (IrO_2) are the most preferred catalysts for OER due to their low overpotential for OER.[4,5] However, the global low reserves and high costs of these metals limit their use on an industrial scale. To overcome these issues, scientists have come up with low-cost transition metal hydroxides/oxides, phosphides, and sulfides which have shown better performance in water electrolysis.[6–9] More specifically, the transition metals, particularly Co, Ni, Fe, and Mn-based materials, are being considered owing to their superior OER performance for potentially outperforming catalysts based on noble metals.[10,11] To be practically advantageous, the catalyst needs to remain stable while approaching high current densities (up to 200 mA cm^{-2}) by incurring low overpotentials. Thus, it is essential to investigate the electrocatalyst, which will operate at high current densities and need very little overpotential.

Amongst various transition metal compounds, nickel/cobalt-based hydroxide and oxides have been extensively studied for electrochemical water splitting owing to their multiple oxidation states, high active sites, high stability, spinel structure, high abundance, and low cost.[12,13] However, their intrinsic insulating nature limits their practical use.[14] Thus, various supports, such as Ni-foam, carbon cloth, carbon black, *etc.*, have been used to increase the conductivity of the material.[15,16] These kinds of supports provide electric pathways to nanoparticles, prevent agglomeration during the electrolysis of water, and increase the efficiency of catalyst utilization.[17,18] Additionally, to

[a]*National Centre for Nanosciences and Nanotechnology, University of Mumbai, Kalina, Mumbai-400098, India. E-mail: pradipsarawade@yahoo.co.in*

[b]*Department of Physics, University of Mumbai, Kalina, Mumbai-400098, India*

[c]*CSIRO Energy, Private Bag 10, Clayton South 319, Victoria, Australia. E-mail: dattatray.dhawale@csiro.au*

[d]*Academy of Scientific and Innovative Research, CSIR-Human Resource Development Center (CSIR-HRDC) Campus, Postal Staff College Area, Ghaziabad, Uttar Pradesh, 201002, India*

[e]*Electronic Structure Theory Group, Physical and Materials Chemistry Division, CSIR-National Chemical Laboratory, Pune, 411008, India*

† Electronic supplementary information (ESI) available. See DOI: https://doi.org/10.1039/d2se01111e

catalyze the OER process, it is important to design the catalyst with a very high specific and active surface area and optimal electrical conductivity. Various approaches have emerged to improve the catalytic activity, such as tuning the morphology of the material, elemental doping, and interfacial engineering.[19–23] Hierarchical structures generally offer higher surface area and active sites and provide better catalytic performance.[24] Materials with hierarchical architectures have been extensively utilized for electrochemical applications due to the fast diffusion of ions and acceleration of surface reaction during electrolysis.[25] Moreover, 3D architectures composed of 1D nanostructures are more beneficial in water-splitting reactions. Such complex structures promote the release of gas bubbles and display enhanced catalytic performance. Thus, it is of great interest to design such 3D hierarchical assemblies which consist of 1D nanostructures, thus making the water oxidation process more efficient.

Spinel AB_2O_4 has been considered a promising, efficient, and stable candidate for promoting water oxidation in alkaline solution. In this spinel structure, A and B occupy a combination of tetrahedral and octahedral sites with different oxidation states.[26] A spinel $NiCo_2O_4$ has shown eye-catching potential in energy storage and energy conversion applications due to the existence of rich multiple oxidations states wherein, Ni^{2+} occupies the tetrahedral (T_d) sites with e_g^4 t_{2g}^4 electronic configuration, and Co^{3+} occupies the octahedral (O_h) sites with e_g^0 t_{2g}^6 electronic configuration.[27,28] The partially filled 3d orbitals in the spinel structure play a key role in generating outstanding electrochemical properties by facilitating the electron transfer process. Experimental observations and theoretical analysis have been performed to identify the active centers and role of contributing orbital.[29,30] For instance, Baglio *et al.* suggested that the Co^{3+} and Ni^{3+} were accountable for better OER performance of $NiCo_2O_4$.[31] Shanmugam and coworkers reported that the high concentration of Ni^{3+} in the $NiCo_2O_4$ electrode material enhanced the electrochemical performance.[32] Liu *et al.* established improved OER performance by engineering NiO with Ni^{3+} ions.[33] Thus, the determination of surface-active species with their oxidation states that are responsible for enhancing the catalytic activity becomes a significant interest. By employing physicochemical characterization tools such as X-ray photoelectron spectroscopy and cyclic voltammetry with low scan rates, the oxidation states of the surface-active species could be determined.

To develop a low-cost, efficient and stable OER electrocatalyst, we describe a facile approach to prepare hierarchical teddy bear sunflower-like $NiCo_2O_4$, spherical NiO, and sea-urchin-like Co_3O_4 using the surfactant-assisted solvothermal procedure. The prepared mesoporous hierarchical teddy bear sunflower-like $NiCo_2O_4$/NF catalyst displayed excellent water oxidation performance even at high current densities. To drive the current densities of 10 mA cm^{-2}, 50 mA cm^{-2}, and 200 mA cm^{-2}, the $NiCo_2O_4$/NF catalyst requires low overpotential of 290 mV, 319 mV and 330 mV, respectively. Furthermore, the electronic structure and charge transport mechanism of all three structures were systematically investigated by assessing density functional theory (DFT) and supported by experimental studies. The developed highly efficient OER catalyst by facile solvothermal route holds great potential for large-scale industrial applications.

2. Experimental

2.1 Materials

Nickel(II) nitrate hexahydrate ($Ni(NO_3)_2 \cdot 6H_2O$), cobalt(II) nitrate hexahydrate ($Co(NO_3)_2 \cdot 6H_2O$), urea ($CO(NH)_2$), cetyltrimethylammonium bromide ($CH_3(CH_2)15N(CH_3)_3Br$) (CTAB), cyclohexane (C_6H_{12}), and 5 wt% Nafion dispersion D520 were purchased from Sigma-Aldrich. All materials used in the synthesis and electrochemical testing were of analytical grade and used as received without further purification.

2.2 Synthesis of $NiCo_2O_4$, NiO, and Co_3O_4 catalysts

For the synthesis of the $NiCo_2O_4$ catalyst, $Co(NO_3)_2 \cdot 6H_2O$ and $Ni(NO_3)_2 \cdot 6H_2O$ metal precursors were used in a solvothermal method. At first, $CO(NH)_2$, 0.66 M, and CTAB, 0.20 M were mixed in cyclohexane (C_6H_{12}, 35 mL). In 35 mL of distilled water, the metal precursors having 0.177 M of $Co(NO_3)_2 \cdot 6H_2O$ and 0.190 M $Ni(NO_3)_2 \cdot 6H_2O$, were dissolved. A homogeneous mixture is obtained by adding precursor solution into cyclohexane by continuous stirring at 400 rpm for about 30 min. The solvothermal reaction was conducted in a hot-air oven at 120 °C for 4 h. The gained products in the powder form were then washed and dried in the air in an oven at 60 °C for 8 h followed by annealing at 450 °C for 4 h in the air to get the $NiCo_2O_4$ phase. The NiO and Co_3O_4 samples are prepared by the previously reported method.[34,35] The Co_3O_4 and NiO catalysts were solvothermal synthesized using $Co(Cl)_2 \cdot 6H_2O$, 0.177 M and $Ni(NO_3)_2 \cdot 6H_2O$, 0.177 M metal precursors, respectively. Both reactions were carried out by keeping all other preparative parameters invariant as that of the $NiCo_2O_4$ catalyst. The prepared catalysts were then used for further structural and surface analysis, followed by water oxidation performance investigations.

2.3 Characterization details

The prepared samples were analyzed by employing various structural and surface characterization techniques. The morphology of the samples was studied with scanning electron microscopy (FE-SEM, JSM-7600F, JEOL). Transmission electron microscopy (TEM, JEM 2100, 200 kV) was used to determine the microstructure of the samples. The lattice spacings in the crystal structure were determined by high-resolution transmission electron microscopy (HR-TEM, JEM 2100, 200 kV). The selected area electron diffraction (SAED) patterns were acquired using the same HR-TEM machine. EDX and elemental mapping were acquired by STEM-EDX JEM-F200(URP). The crystallinity and phase of the samples were determined using a powder X-ray diffractometer (XRD) (Rigaku Ultima IV) with Cu-kα irradiation. X-ray photoelectron spectroscopy (XPS, K ALPHA Thermo Fisher, Al Kα) was utilized to investigate the surface chemistry of the catalysts. With the help of Avantage software, the concentration of surface atoms of the prepared samples was estimated.

Brunauer–Emmett–Teller (BET) surface area analyzer (Micromeritics ASAP 2000) was utilized to obtain the N_2 adsorption–desorption isotherm and physical surface area.

2.4 DFT calculations

The *ab initio* modeling is performed using Quantum ESPRESSO (QE).[36,37] The projector augmented wave method (PAW) is used for calculations to describe the ion–electron interaction. A primitive cell of normal spinel of $Ni_2Co_4O_8$ (contains two formula units) is used with a wave function cut-off of 90 Ry to truncate the plane wave expansion. The energy cut-off was set to 10^{-6} Ry, and the cut-off for forces was set to 10^{-4} Ry bohr^{-1}. Spin-polarized density functional theory (DFT) calculations are performed using generalized gradient approximation in which Perdew–Burke–Ernzerhof (PBE) functional describes the exchange and correlation.[38] Dudarev *et al.* proposed the use of Hubbard U correction to account for the correlation effect between 3d electrons of transition metals.[39] Thus, we first benchmark the value of Hubbard U correction for Ni and Co. We get an energy minimum for U values of 3.0 and 1.6 for Co and Ni, respectively. The *k*-mesh of $7 \times 7 \times 7$ is used for geometry optimization of $NiCo_2O_4$, and $14 \times 14 \times 14$ is used for density of state (DOS) and partial-DOS (pDOS) calculations. The high symmetry points are generated based on Aflow.[40]

2.5 Electrochemical study

The electrochemical water oxidation performance was investigated using linear scale and cyclic voltammetry (CV) techniques. Three-electrode system attached to the Autolab electrochemical workstation was used for electrochemical measurements. Initially, catalyst powder (5 mg) was dissolved in a mixture of Nafion (25 μL) and ethanol (1 ml), and the solution was sonicated for 10 min. Then 20 μL of prepared ink was drop cast onto the 1 cm^2 surface of the nickel foam electrode (NF) with a mass loading of about 0.1 mg cm^{-2} and dried under the infra-red lamp and used as a working electrode. The Pt wire and Ag/AgCl filled with 3 M KCl electrolyte were used as counter and reference electrodes, respectively. The linear sweep voltammetry (LSV) scans were acquired at a scan rate of 1 mV s^{-1} in the potential window of 0 V to 0.8 V *vs.* Ag/AgCl. The CV curves at the various scan rates (40, 60, 80, 100, and 120 mV s^{-1}) were recorded in the potential window of −0.01 to 0.05 V *vs.* Ag/AgCl before the redox reaction occurs to estimate the double-layer capacitance (C_{dl}) and the electrochemically active surface area (ECSA). The obtained potentials were calculated with respect to the reversible hydrogen electrode (RHE) by using the Nernst equation: $E_{RHE} = E_0 + (0.059 \times pH)$.

3. Results and discussion

Fig. 1 depicts the fabrication method of the $NiCo_2O_4$ sample. The $NiCo_2O_4$ is synthesized with the facile solvothermal method in which cationic surfactant (CTAB) plays an important role. As given in the Experimental section, a 1 : 1 ratio of cobalt nitrate and nickel nitrate was used for the synthesis of $NiCo_2O_4$ composition. Initially, with increasing temperature, urea decomposes and produces OH^- ion. The Co^{2+} and Ni^{2+} ions react with hydroxide ions which are liberated from urea and generate a Ni–Co hydroxide composite. Next, the Ni–Co hydroxide composite gets arranged in a teddy bear sunflower-like spherical structure wherein several nano spines grown from the center could be observed.[41] Lastly, after the annealing process, hydroxides of metal decompose completely and form

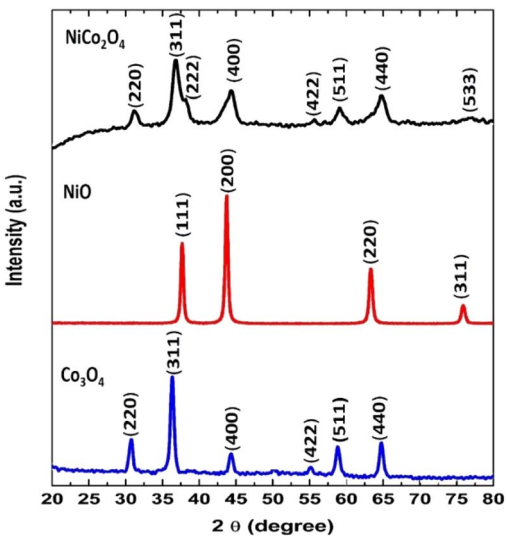

Fig. 2 Indexed powder XRD patterns of $NiCo_2O_4$, NiO and Co_3O_4 samples.

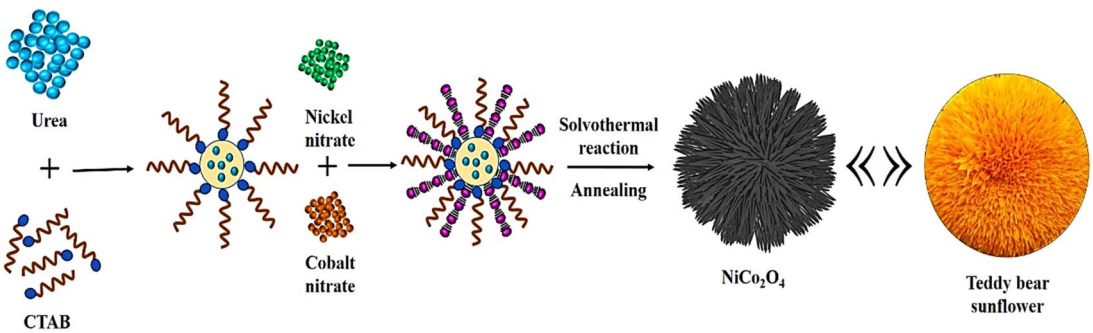

Fig. 1 Schematic representation for the synthesis of hierarchical teddy bear sunflower-like $NiCo_2O_4$ catalyst.

crystalline $NiCo_2O_4$ metal oxide. It can be seen from Fig. 1 that a well-defined hierarchical teddy bear sunflower structure of $NiCo_2O_4$ catalyst is obtained. The surfactant (CTAB) plays a significant role in the growth mechanism of such spherical structures along with reaction parameters.[42–44] The cationic surfactant CTAB contains a hydrophilic polar head and a hydrophobic tail giving rise to the spherical micellar structure. During the reaction, the inorganic anions from the cobalt salt and nickel salt intrinsically adsorbed on the surfactant and thus directed the final morphology. The final shape of the catalyst depends on the exact conditions of the synthesis. Consequently, a combination of different metal precursors and CTAB

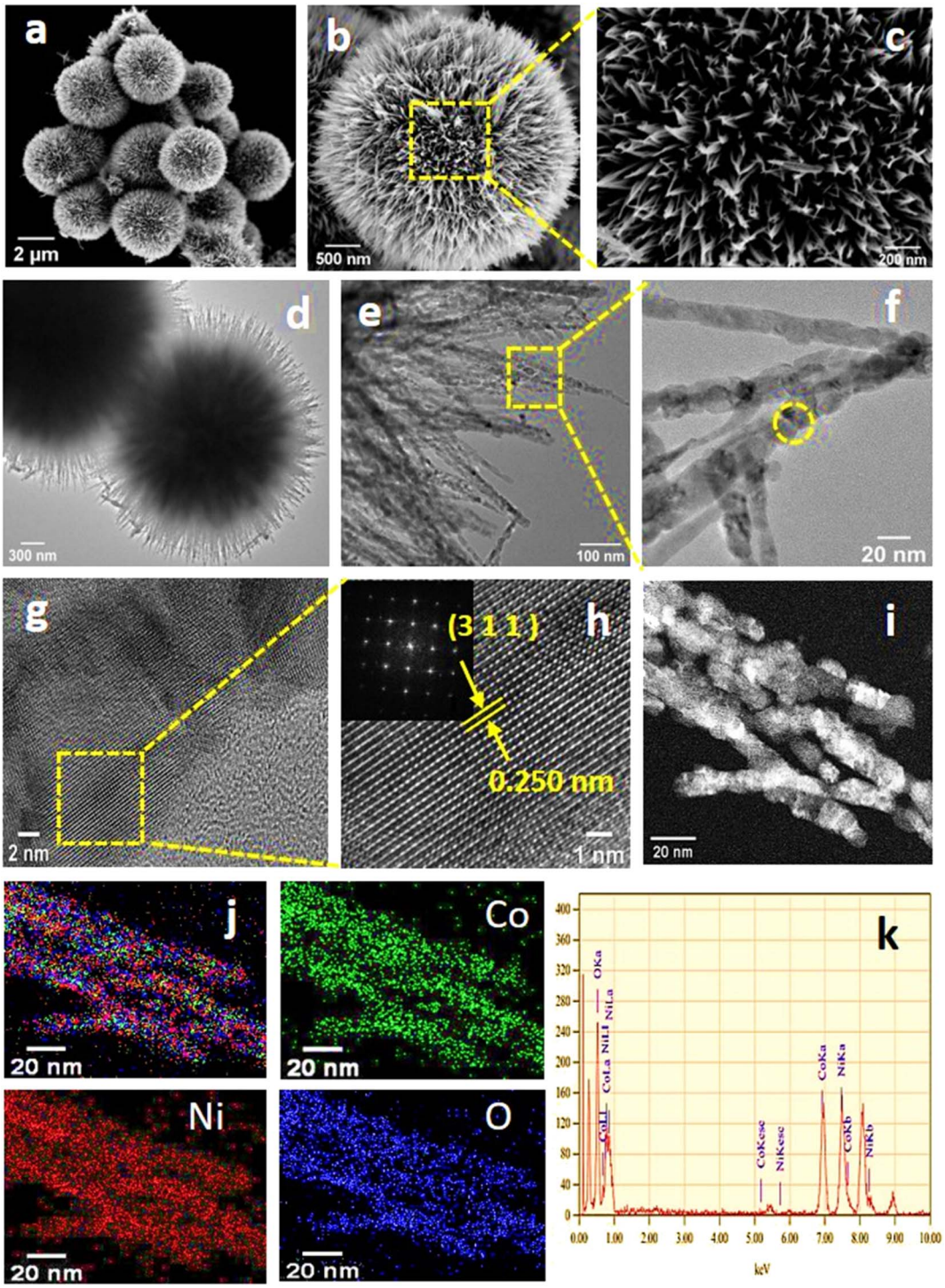

Fig. 3 Low and high magnification FE-SEM images of hierarchical teddy bear sunflower-like $NiCo_2O_4$ (a–c, respectively). Low and high magnification TEM images of $NiCo_2O_4$ (d–f, respectively). HR-TEM (g and h), and STEM image (i), respectively. STEM-elemental mapping of Co, Ni, and O with an overlay of all three elements (j). EDX of $NiCo_2O_4$ (k).

formulates diverse morphologies. The NiO and Co_3O_4 have followed a similar mechanism in forming spherical and sea-urchin-like structures, respectively.

The phase identification and the structure investigation of the prepared $NiCo_2O_4$, NiO, and Co_3O_4 samples were carried out using X-ray powder diffraction (XRD) analysis (Fig. 2). The prepared $NiCo_2O_4$ and Co_3O_4 samples exhibit FCC cubic spinel structure. The observed diffraction peaks match well with the JCPDS file no. 20-0781 for $NiCo_2O_4$ and JCPDS, no. 42-1467 for Co_3O_4.[30,45] The smallest average crystallite size was obtained for $NiCo_2O_4$ (5.4 nm), which was determined by the Debye–Scherrer equation (Table S1†). The XRD pattern of the NiO sample show peaks indexed to the pure phase of FCC NiO (JCPDS file no. 78-0643).[46] The cubic lattice constants for $NiCo_2O_4$, Co_3O_4, and NiO samples (Table S1†) are obtained from high-intensity peaks and are in accordance with the theoretical values indicating high phase purity of all the prepared samples.[47]

The surface morphology of the $NiCo_2O_4$ catalyst was investigated by FE-SEM, displayed in Fig. 3(a)–(c). From low-magnification FE-SEM images (Fig. 3(a) and (b)), we can observe that the prepared $NiCo_2O_4$ sample displays uniform microspheres (4 μm diameter). The high-magnification FE-SEM image (Fig. 3(c)) depicts that these microspheres are composed of several nano spines with a length of 1 μm. The TEM image of the $NiCo_2O_4$ sample (Fig. 3(d)) agrees well with the obtained FE-SEM image. The nano spines in the $NiCo_2O_4$ are made up of numerous nanoparticles with diameters of 14–18 nm and resemble teddy bear sunflowers, as revealed by high-magnification TEM images (Fig. 3(e) and (f)). These nanoparticles interconnect and form the porous teddy bear sunflower-like structure that exhibits a high specific surface area. Such porous structures may adsorb enough oxygen and offer more active sites.[48] Fig. 3(g) displays the HRTEM image of encircled region of Fig. 3(f). The enlarged view (Fig. 3(h)) reveals the lattice plane with a spacing of 0.25 nm attributed to the (3 1 1) plane of the $NiCo_2O_4$ phase.[49] The inset of Fig. 3(h) depicts the SAED pattern of the hierarchical teddy bear sunflower-like $NiCo_2O_4$ catalyst, which indicates the polycrystalline nature of the prepared catalyst and could be indexed to the spinel phase of $NiCo_2O_4$. The STEM-EDS spectra and mapping of the $NiCo_2O_4$ shows the even distribution of the Ni, Co, and O elements on the surface, shown in Fig. 3(i) and (j), respectively. FE-SEM images of NiO and Co_3O_4 samples exhibit spherical and sea-urchin-like morphology, which are displayed in Fig. S1(a) and (b).†

The oxidation states and elemental composition of hierarchical teddy bear sunflower-like $NiCo_2O_4$, spherical NiO, and sea-urchin-like Co_3O_4 samples were investigated using the X-ray photoelectron spectroscopy technique (Fig. 4 and S2(a)–(f)†) and the analysis data is shown in Table S2.† The presence of

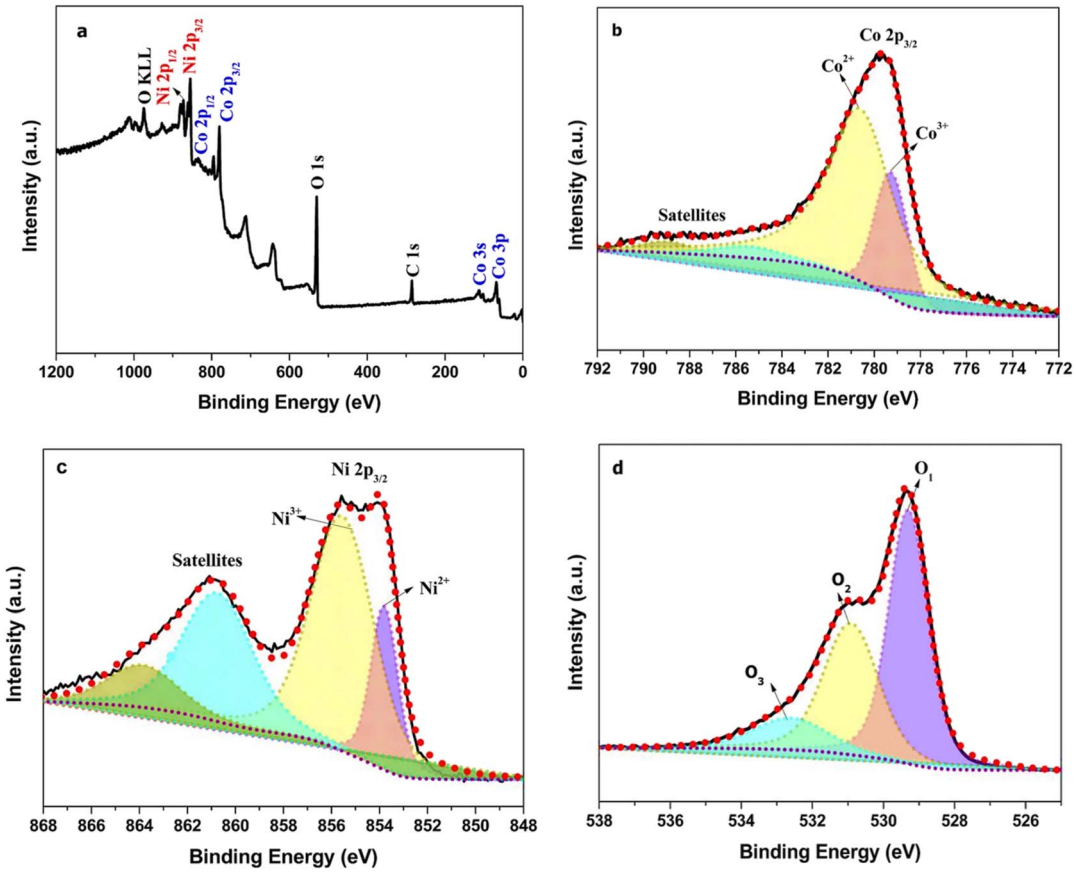

Fig. 4 XPS survey scan of hierarchical teddy bear sunflower $NiCo_2O_4$ catalyst (a), high-resolution XPS spectra for Co 2p, Ni 2p, and O 1s states in $NiCo_2O_4$ (b–d, respectively).

only Ni, Co, and O elements in the survey spectrum (Fig. 4(a)) of the hierarchical teddy bear sunflower-like $NiCo_2O_4$ sample is in line with the STEM-EDX spectrum (Fig. 3(k)). The deconvoluted (Gaussian) Co $2p_{3/2}$, Ni $2p_{3/2}$, and O 1s XPS spectrum are shown in Fig. 4(b)–(d), respectively. The high-resolution Co $2p_{3/2}$ spectrum in Fig. 4(b) establishes that spin-doublets were attributed to Co^{3+} and Co^{2+}.[50] These characteristic peaks are also accompanied by Co $2p_{3/2}$ satellite peaks. Fig. 4(c) shows the high-resolution Ni $2p_{3/2}$ XPS spectrum. The binding energy peaks attributed to the Ni^{3+} $2p_{3/2}$ and Ni^{2+} $2p_{3/2}$, respectively.[50,51] These oxidation states of Ni and Co in $NiCo_2O_4$ are compared with the Ni 2p and Co $2p_{3/2}$ line shapes from NiO and Co_3O_4 samples (Fig. S2(b) and (e)†, respectively) and it is observed that both Ni $2p_{3/2}$ and Co $2p_{3/2}$ in $NiCo_2O_4$ sample exhibit a small upward shift of 0.3 eV and extra-large shift of 1.1 eV towards higher binding energy, respectively indicates the significant electron donors adjacent to Co. A remarkable increase in the intensity ratio for Ni^{3+}/Ni^{2+} was observed in $NiCo_2O_4$ (Fig. 4(c)) as compared to NiO (Fig. S2(b)†). Whereas no such change is detected in the case of Co oxidation states when compared to Co_3O_4. This directs that a large amount of Ni^{2+} ions were oxidized to Ni^{3+}. The XPS spectrum for O 1s can be deconvoluted into three peaks which can be related to the lattice oxygen (O_I), surface absorbed hydroxyl (O_{II}), and surface C–O(O_{III}), respectively (Fig. 4(d)).[52–54] The peak that appeared in the O 1s state of $NiCo_2O_4$ at 530.98 eV was ascribed to the coordination of oxygen–Ni^{2+}, signifying the maximum Ni^{2+} content on the surface of the hierarchical teddy bear sunflower-like $NiCo_2O_4$ catalyst.[54] Thus, the existence of high valence states of the metal cations as well as oxygen adsorption species endows the hierarchical teddy bear sunflower-like $NiCo_2O_4$ catalyst with greater electrical conductivity and rapid charge transport for water splitting.

Brunauer–Emmett–Teller (BET) study was performed for the hierarchical teddy bear sunflower-like $NiCo_2O_4$, spherical NiO, and sea-urchin-like Co_3O_4 samples to examine the surface area, shown in Fig. S3.† BET surface area of $NiCo_2O_4$ and NiO and Co_3O_4 catalysts were measured to be 100.79 $m^2\ g^{-1}$, 68.53 $m^2\ g^{-1}$, and 59.76 $m^2\ g^{-1}$, respectively. The marginal difference in surface areas and morphologies suggests the large variety of surface areas contributes more to enhancing OER activities in $NiCo_2O_4$ and NiO and Co_3O_4 catalysts discussed in the following. The prominent hysteresis of type IV H3 was observed for the hierarchical teddy bear sunflower-like $NiCo_2O_4$ sample, demonstrated by BET adsorption–desorption. It is well established that the larger specific surface area of the catalyst provides more electroactive sites for the faradaic reactions.[55,56] This high surface area of $NiCo_2O_4$ and well-defined nanoparticles can promote water oxidation performance effectively.

4. DFT calculation for density of states (DOS)

Before directly measuring the water oxidation performance of all three samples, we carried out a DFT calculation to gain the DOS statistics at the surface of each sample. To understand the

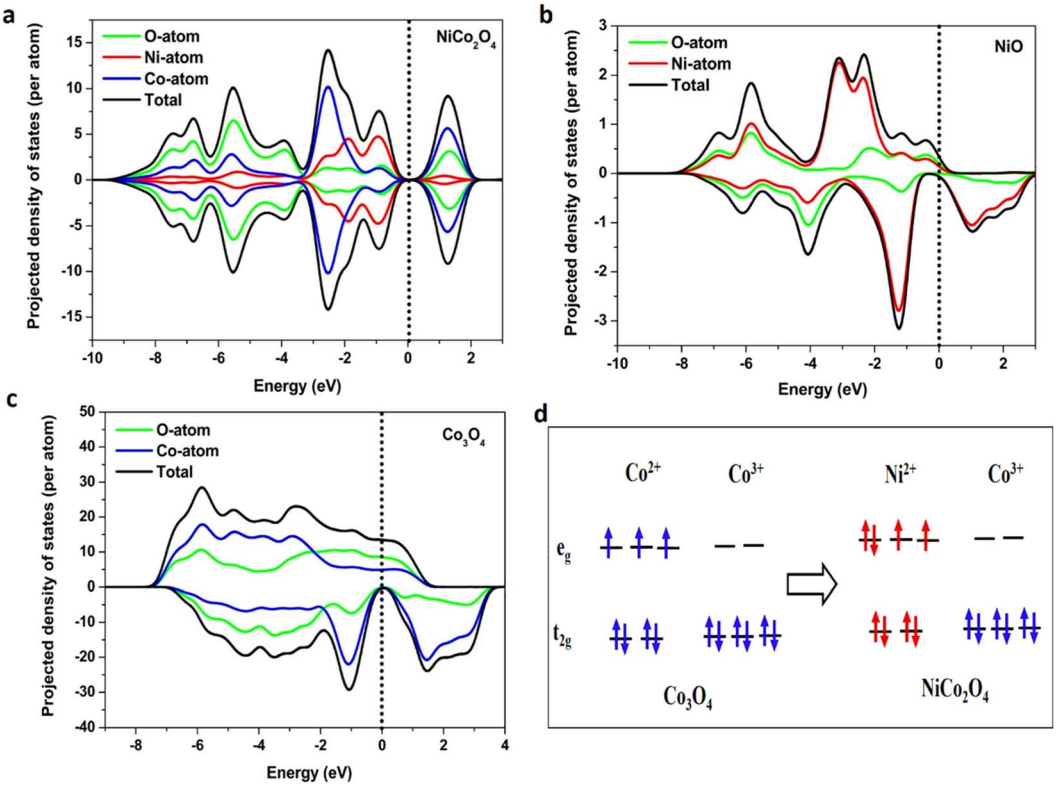

Fig. 5 The partial and total projected density of states for $NiCo_2O_4$ (a), NiO (b), and Co_3O_4 (c), respectively, calculated using density functional theory (DFT)+U, (d) schematic diagram of the spin-states in the Co_3O_4 in the left and $NiCo_2O_4$ in the right.

contribution of different orbitals in catalyzing the OER process, we analyze the projected density of states (pDOS). A series of pDOS plots with up and down spins for $NiCo_2O_4$, NiO, and Co_3O_4 materials are shown in Fig. S4(a)–(d).† The partial and total DOS for $NiCo_2O_4$, NiO, and Co_3O_4 materials are shown in Fig. 5(a)–(c). We observed that a major contribution to the up-channel comes from the p orbitals of the O atom followed by the d-orbital of the Co atom in Co_3O_4 (Fig. S4(d)†). The contribution of O-p up-spin orbitals is almost twice that of Co-d up-spin orbitals. In NiO no significant contribution from the up-channel was detected (Fig. S4(c)†).

In $NiCo_2O_4$, the up spin and down spin of each atom contribute equally to the entire system (Fig. 5(a)), indicating the composite effect in the electronic system. The 3d-orbitals from Ni atoms show a higher density of states near the Fermi level (E_f) than Co-2d (Fig. S4(a)†) in $NiCo_2O_4$. Our calculation shows that DOS around E_f is dominated by the Ni^{2+} cations occupying the tetrahedral sites. Fig. 5(d) shows the predicted electron occupation in d orbitals for the spinel Co_3O_4 and $NiCo_2O_4$ systems based on the oxidation states. The new electronic state is present in the conduction band of $NiCo_2O_4$ (Fig. 5(d)), indicating that more electrons are available to participate in the catalytic process. The electronic states prediction is compared with the literature, which matches our theoretical calculations and experimental results.[47,57] The d-orbital occupancy integrated from the DOS results is presented in Table S3,† which is close to our prediction of electronic configuration. Hence, we postulate that the Ni atom has a major contribution to catalytic activity, whereas the Co atom is responsible for conductivity in $NiCo_2O_4$ material.

5. Water oxidation performance

The fabricated hierarchical teddy bear sunflower-like $NiCo_2O_4$, spherical NiO, and sea-urchin-like Co_3O_4 catalysts supported on nickel foam were subjected to electrochemical water oxidation performance through OER in 1 M KOH alkaline electrolyte as shown in Fig. 6. The OER performances of the $NiCo_2O_4$/NF, NiO/NF, and Co_3O_4/NF are evaluated by LSV polarization curves (Fig. 6(a)) at a scan rate of 1 mV s^{-1} after 15 cycles of CV measurement. The superior OER performance was observed for the hierarchical teddy bear sunflower-like $NiCo_2O_4$/NF catalyst ($\eta_{10} = 290$ mV) as compared to the spherical NiO/NF ($\eta_{10} = 300$ mV), the sea-urchin-like Co_3O_4/NF ($\eta_{10} = 322$ mV), and commercial RuO_2 ($\eta_{10} = 335$ mV) to achieve a current density of 10 mA cm^{-2}. The overpotential values with respect to different current densities (10 mA cm^{-2}, 50 mA cm^{-2}, and 200 mA cm^{-2}) for $NiCo_2O_4$/NF, NiO/NF, and Co_3O_4/NF catalysts are plotted and presented in Fig. 6(b). The enhanced catalytic activity of $NiCo_2O_4$/NF catalyst relative to NiO/NF and Co_3O_4/NF is attributed to the porous hierarchical nanostructure exhibited by $NiCo_2O_4$/NF, which could provide high surface area and abundant active sites also facilitating the fast ion transport kinetics. Concerning the impinge of specific surface area on the intrinsic activity, BET surface area normalized LSV was plotted (Fig. S5†). The observed OER activity trend was similar to that of LSV concerning the geometrical surface area. Furthermore, as shown in Fig. 6(c), the hierarchical teddy bear sunflower-like $NiCo_2O_4$/NF catalyst exhibited the ultralow Tafel slope value of 37 mV dec^{-1}, which is substantially smaller than the spherical NiO/NF (52 mV dec^{-1}) and the sea-urchin like Co_3O_4/NF (96 mV dec^{-1}). The low Tafel slope value in the case of the hierarchical teddy bear sunflower-like $NiCo_2O_4$/NF catalyst indicates the facile charge transport at the interface.

The electrochemical active surface area (ECSA) of electrocatalysts plays an imperative role in evaluating the activity of the catalyst.[58] The ECSA was evaluated by dividing the obtained double-layer capacitance (C_{dl}) value by the specific capacitance (C_s) of the catalyst. To determine the C_{dl} of all three catalysts, CVs were obtained in the non-faradaic potential region at different scan rates (Fig. S6†). As shown in Table S4,† it illustrates that the C_{dl} of the hierarchical teddy bear sunflower-like $NiCo_2O_4$/NF, spherical NiO/NF, and sea-urchin-like Co_3O_4/NF catalysts are 1.68, 1.07, and 0.69 mF cm^{-2}, respectively and presented in Fig. 6(d). The C_s value of 26 μF cm^{-2} and 25 μF cm^{-2} and 27 μF cm^{-2} are used to calculate the ECSA of hierarchical teddy bear sunflower-like $NiCo_2O_4$/NF, spherical NiO/NF, and sea-urchin Co_3O_4/NF catalysts.[59] The higher ECSA of 64.61 cm^2 for hierarchical teddy bear sunflower-like $NiCo_2O_4$ catalyst compared to spherical NiO/NF (42.8 cm^2), and sea-urchin Co_3O_4/NF (25.55 cm^2) catalysts confirms the close correlation between active sites and surface morphology. The electrochemical impedance spectroscopy (EIS) was conducted at a potential of 1.536 V *vs.* RHE in the frequency range of 0.01–100 kHz for all three catalysts to extract the charge transfer kinetics at the electrode–electrolyte interface. The Nyquist plots and the fitted equivalent circuit composed of a charge transfer resistance (R_{ct}), electrolyte resistance (R_s), and an electrical double-layer capacitance (C_{dl}) are shown in Fig. 6(e) and inset of Fig. 6(e), respectively. The capacitance and resistance values are calculated and tabulated in Table S4.† The low R_{ct} value of 1.15 Ω cm^2 for hierarchical teddy bear sunflower-like $NiCo_2O_4$ compared to the other catalysts suggests a significantly higher charge-transfer kinetics resulting in enhanced OER performance.

The redox reactions for the hierarchical teddy bear sunflower-like $NiCo_2O_4$/NF, spherical NiO/NF, and sea-urchin-like Co_3O_4/NF catalysts were investigated to understand the surface reactivity by employing CVs between 1.036 to 1.836 V *vs.* RHE at a sweep rate of 2 mV s^{-1} in 1 M KOH (Fig. S7†). A pair of redox peaks were noticed in all three catalysts. The redox peaks are principally ascribed to the formation of MO/MOOH (M denotes Co/Ni/NiCo ions) reaction intermediate in the faradaic process.[60,61] The occurrence of a single anodic oxidation peak at 1.38 V *vs.* RHE for both $NiCo_2O_4$/NF and NiO/NF catalysts attributed to the Ni^{2+}/Ni^{3+} transition, confirming that a large amount of Ni^{2+} ions were oxidized to Ni^{3+} ions which is consistent with the XPS analysis.[62] The sharp cathodic peaks at 1.29 V *vs.* RHE are observed for NiO/NF and $NiCo_2O_4$/NF catalysts, respectively.[63] Moreover, both the surface analysis techniques (XPS and CV) revealed that the Ni cations are present in large amounts on the surface of $NiCo_2O_4$/NF catalyst compared to Co cations demonstrating that the Ni cations are mainly

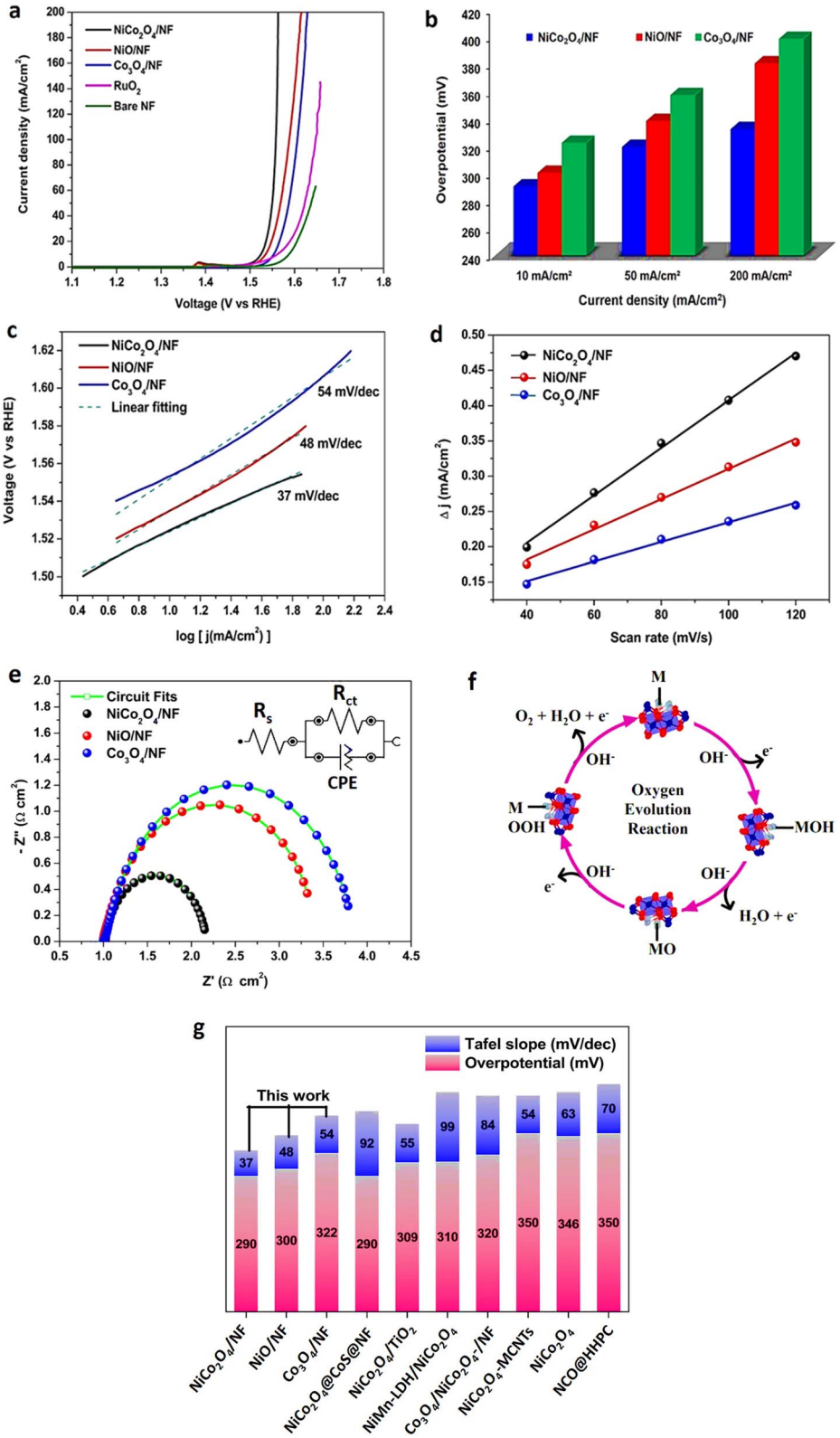

Fig. 6 (a) Linear polarization curves at a scan rate of 1 mV s^{-1} $NiCo_2O_4$/NF, NiO/NF, Co_3O_4/NF, RuO_2, and bare NF catalysts for OER. (b) Overpotential *vs.* current density plot of $NiCo_2O_4$/NF, NiO/NF, and Co_3O_4/NF catalysts. (c) Tafel plots of $NiCo_2O_4$/NF, NiO/NF, and Co_3O_4/NF. (d) Plot representing the relationship between the difference in the anodic and cathodic current densities and scan rate. The slope of the fitted line is the double-layer capacitance (C_{dl}) of $NiCo_2O_4$/NF, NiO/NF, and Co_3O_4/NF catalysts. (e) Electrochemical impedance spectra (Nyquist curves) of $NiCo_2O_4$/NF, NiO/NF, and Co_3O_4/NF catalysts; the inset shows the equivalent circuit for the data. (f) Schematic of the four-step reaction pathway for OER in alkaline electrolyte. (g) Comparison of the overpotential (η_{10}) and Tafel slopes for the catalyst prepared in this work and recently reported $NiCo_2O_4$.

responsible for enhanced OER performance by forming NiOOH as a reaction intermediate and provide more active sites.[50,54]

Another influential parameter for catalyst performance evaluation is mass activity (MA). To eradicate the impact of mass loading, MA was determined by normalizing the current density with the mass loading of the material on the surface of the electrode.[64] The MA values of 140 A g^{-1}, 95 A g^{-1}, and 44 A g^{-1} are obtained at a potential of 1.53 V *vs.* RHE for the hierarchical teddy bear sunflower-like $NiCo_2O_4$/NF, spherical NiO/NF, and sea-urchin-like Co_3O_4/NF catalyst, respectively. Manifestly, the trend is in good agreement with that of overpotential values for all three catalysts. Higher specific and mass activities of the hierarchical teddy bear sunflower-like $NiCo_2O_4$/NF catalyst reflect the higher electrocatalytic activity as compared to the other two catalysts (NiO/NF and Co_3O_4/NF). To further evaluate the efficiency of prepared catalysts, turnover frequency (TOF) values which is the measure of intrinsic activity were determined.[65] Considering that all of the available surface metal atoms are catalytically active, TOF at a fixed potential of 1.53 V *vs.* RHE was determined as 0.61 s^{-1}, 0.26 s^{-1}, and 0.18 s^{-1} for the $NiCo_2O_4$/NF, NiO/NF, and Co_3O_4/NF catalysts, respectively, further suggesting that the hierarchical teddy bear sunflower-like $NiCo_2O_4$/NF is indeed an efficient and potent catalyst.

5.1 Correlation of the OER activity with electronic states in different structures

Herein, the theoretical calculations and experimental study complement each other for the study of OER mechanisms from the perspective of thermodynamics and kinetics. The water oxidation reaction in an alkaline solution is expressed as;

$$4OH^- \rightarrow O_{2(g)} + 2H_2O_{(l)} + 4e^- \quad (1)$$

This specific water oxidation process of OER can be described in terms of the adsorbate evolution mechanism (AEM) with four elementary steps as follows (Fig. 6(f));[66]

$$M + OH^- \rightarrow MOH + e^- \quad (2)$$

$$MOH + OH^- \rightarrow MO + H_2O + e^- \quad (3)$$

$$MO + OH^- \rightarrow MOOH + e^- \quad (4)$$

$$MOOH + OH^- \rightarrow MO_2 + H_2O + e^- \quad (5)$$

where MOH, MO and MOOH represent adsorbed reaction intermediates with metal surface site M. Notably, the XPS and slow scan CV investigation provide evidence for the existence of more active Ni^{3+} cations than Co on the surface of $NiCo_2O_4$ to trigger the formation of NiOOH which was critical for enhancing OER. Certainly, the above-analyzed DFT results manifest that the morphology of the material has a considerable effect on the electronic structure near the E_f of the electrocatalysts. Co_3O_4 has a normal spinel structure, where Co^{2+} is located at tetrahedral (T_d) sites and Co^{3+} at (O_h) sites; however, $NiCo_2O_4$ has an inverse spinel structure, where preferably Ni^{2+} occupies O_h sites and Co^{3+} occupies both O_h and T_d sites. Nevertheless, Co^{3+} at T_d sites is thermodynamically unstable and likely to convert to a more stable Co^{2+} state. This results in the oxidation of a similar amount of Ni^{2+} to Ni^{3+} to sustain charge neutrality. Therefore, the electronic state induced by morphology is the key to describing enhanced OER activity in $NiCo_2O_4$. According to the Gerischer–Marcus model of charge transfer, orbital overlapping occurs due to the high DOS near the E_f which then could adsorb OH^- species and reduce the energy to accept or donate electrons at the adsorbate–catalyst interface reaction.[67] As mentioned above, 3D nanostructure morphology in $NiCo_2O_4$ exhibits far more active sites and could adsorb higher amounts of OH^- species, also providing a sufficient conduction path to prevent serious ohmic losses demonstrated by EIS investigations and adsorption isotherms. We, therefore, plot the ECSA-corrected LSV curves for all three electrocatalysts (Fig. S8†). It is illustrated that porous nanostructure fairly enhances the intrinsic catalytic activity of $NiCo_2O_4$/NF. Moreover, the higher intrinsic activity with large electron transfer has been witnessed by catalyst utilization measurement. Catalyst utilization is as the ECSA of the active catalyst divided by the BET surface area of the catalyst (see ESI eqn (2)†). The high efficiency of catalyst utilization (64.28%) in $NiCo_2O_4$/NF is attributed to the higher adsorption of OH^- ions and better charge conductivity at the electrode interface (Table S5†).

Of note, all the aforementioned OER activity evaluation parameters, including electroactive surface area, charge transfer resistance, electrical conductivity, catalyst utilization, and TOF (Table 1) values suggest that the $NiCo_2O_4$/NF exhibiting teddy-bear sunflower-like morphology is highly active for the water oxidation process compared to spherical NiO/NF and sea-urchin like Co_3O_4/NF. Such hierarchical nanostructure unveiled by $NiCo_2O_4$/NF achieves high current density at low overpotential and delivers high intrinsic activity owing to facile electrolyte penetration along with the prominently high density of Ni 3d states near the Fermi level. Fig. 6(g) and Table S6† show the comparison of overpotential values at a current density of 10 mA cm^{-2} and Tafel slope for recently reported nickel and cobalt-based bimetallic catalysts.[68–74] It is noteworthy that, the fabricated hierarchical teddy-bear sunflower-like $NiCo_2O_4$/NF in

Table 1 Summary of catalytic performances for the prepared $NiCo_2O_4$/NF, NiO/NF, and Co_3O_4/NF electrocatalysts

Electrocatalyst	Overpotential (mV) at 10 mA cm^{-2}	Tafel slope mV dec^{-1}	ECSA m^2 g^{-1}	BET surface area m^2 g^{-1}	Mass activity (mA mg^{-1})	TOF s^{-1}
$NiCo_2O_4$/NF	290	37	64.61	100.79	140	0.61
NiO/NF	300	48	42.40	68.53	95	0.26
Co_3O_4/NF	322	54	25.55	59.76	44	0.18

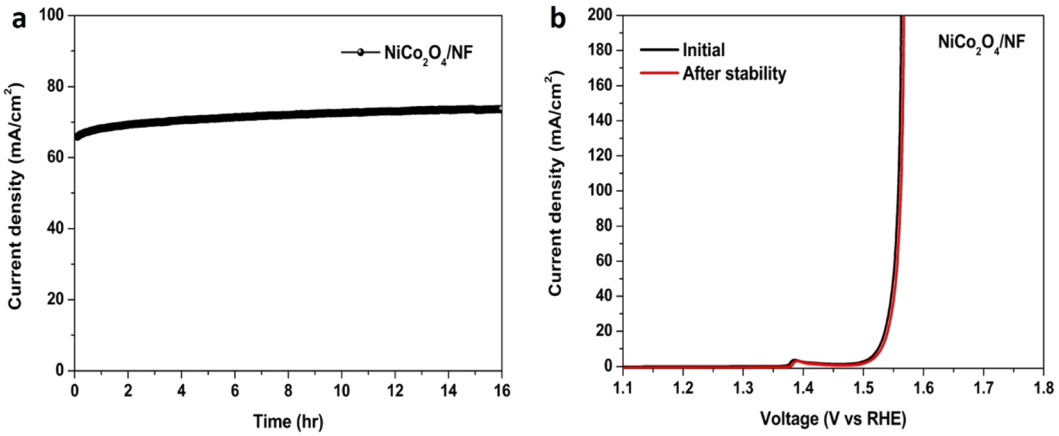

Fig. 7 The chronoamperometric curve at 1.55 V *vs.* RHE of $NiCo_2O_4$/NF catalyst (a), LSV curves of $NiCo_2O_4$/NF catalyst before and after stability for OER in 1 M KOH at a scan rate of 1 mV s^{-1} (b).

this work is the potential low-cost candidate as an OER catalyst for practical applicability in the water-splitting process.

In addition to catalytic efficiency, stability is another important parameter for an OER catalyst. To confirm the stability of the hierarchical teddy bear sunflower-like $NiCo_2O_4$/NF catalyst, chronoamperometry measurement was carried out at 1.55 V *vs.* RHE for 16 h, shown in Fig. 7(a). It clearly indicates that the hierarchical teddy bear sunflower-like $NiCo_2O_4$/NF catalyst is highly stable in 1 M KOH. The LSV at 1 mV s^{-1} for the catalyst was recorded after stability testing and compared with the initial LSV (before stability), shown in Fig. 7(b). The hierarchical teddy bear sunflower-like $NiCo_2O_4$/NF catalyst displayed similar activity even after 16 h (Fig. 7(b)). The morphology of the hierarchical teddy bear sunflower-like $NiCo_2O_4$/NF catalyst after the OER operation was shown in Fig. S9(a)–(d).† The characteristic teddy bear sunflower-like structure was preserved even after 16 h, demonstrating the practical electrocatalytic durability of the product.

6. Conclusions

In summary, we report the fabrication of the hieratical teddy bear sunflower-like $NiCo_2O_4$, spherical NiO/NF, and sea-urchin-like Co_3O_4 using a facile solvothermal and annealing route. A comparative investigation of all three catalysts supported on nickel foam for water oxidation through OER analysis was performed. The hierarchical teddy bear sunflower-like $NiCo_2O_4$/NF catalyst has displayed superior OER activity with a low water oxidation overpotential of 290 mV and 330 mV at respectively 10 mA cm^{-2} and 200 mA cm^{-2} current densities. The enhanced OER performance of the hieratical teddy bear sunflower-like $NiCo_2O_4$ catalyst was mainly attributed to the large specific and active surface area, high catalyst utilization, and high intrinsic activity (TOF). We also investigated the intrinsic contribution of the 3d orbital states of Ni and Co atoms to the OER activity of $NiCo_2O_4$. The practical utilization of the hieratical teddy bear sunflower-like $NiCo_2O_4$/NF was probed through the stability testing of the material. The stable electrochemical performance and sustained morphology, even after prolonged cycling, indicate that the catalyst is highly suitable for the large-scale water oxidation reaction. This work provides a systematic analysis of the structural and electrochemical performance supported by DFT calculation of the prepared catalyst toward their OER counterparts.

Conflicts of interest

There are no conflicts of interest to declare.

Acknowledgements

This work was supported by the Department of Science and Technology-WOS-A scheme (SR/WOS-A/PM-9/2018(G)).

References

1 S. Chu and A. Majumdar, *Nature*, 2012, **488**, 294–303.
2 I. C. Man, H. Y. Su, F. Calle-Vallejo, H. A. Hansen, J. I. Martínez, N. G. Inoglu, J. Kitchin, T. F. Jaramillo, J. K. Nørskov and J. Rossmeisl, *ChemCatChem*, 2011, **3**, 1159–1165.
3 M. W. Kanan and D. G. Nocera, *Science*, 2008, **321**, 1072–1075.
4 Y. Lee, J. Suntivich, K. J. May, E. E. Perry and Y. Shao-Horn, *J. Phys. Chem. Lett.*, 2012, **3**, 399–404.
5 T. Audichon, T. W. Napporn, C. Canaff, C. u. Morais, C. m. Comminges and K. B. Kokoh, *J. Phys. Chem. C*, 2016, **120**, 2562–2573.
6 Y. Liu, H. Jiang, Y. Zhu, X. Yang and C. Li, *J. Mater. Chem. A*, 2016, **4**, 1694–1701.
7 K. Zhang and R. Zou, *Small*, 2021, 2100129.
8 P. M. Bodhankar, P. B. Sarawade, G. Singh, A. Vinu and D. S. Dhawale, *J. Mater. Chem. A*, 2021, **9**, 3180–3208.
9 P. M. Bodhankar, P. B. Sarawade, P. Kumar, A. Vinu, A. P. Kulkarni, C. D. Lokhande and D. S. Dhawale, *Small*, 2022, 2107572.

10 S. Anantharaj, S. R. Ede, K. Sakthikumar, K. Karthick, S. Mishra and S. Kundu, *ACS Catal.*, 2016, **6**, 8069–8097.
11 Z. Peng, D. Jia, A. M. Al-Enzi, A. A. Elzatahry and G. Zheng, *Adv. Energy Mater.*, 2015, **5**, 1402031.
12 D. S. Dhawale, P. Bodhankar, N. Sonawane and P. B. Sarawade, *Sustainable Energy Fuels*, 2019, **3**, 1713–1719.
13 Y. Gao, D. Zheng, Q. Li, W. Xiao, T. Ma, Y. Fu, Z. Wu and L. Wang, *Adv. Funct. Mater.*, 2022, **32**, 2203206.
14 X. Bo, Y. Zhang, M. Li, A. Nsabimana and L. Guo, *J. Power Sources*, 2015, **288**, 1–8.
15 Y. Zhang, J. Yang, Z. Yu, Y. Hou, R. Jiang, J. Huang, F. Yang, S. Yao, L. Gao and W. Tang, *Chem. Eng. J.*, 2021, **416**, 129124.
16 J. Liang, Y.-Z. Wang, C.-C. Wang and S.-Y. Lu, *J. Mater. Chem. A*, 2016, **4**, 9797–9806.
17 K. Artyushkova, S. Pylypenko, M. Dowlapalli and P. Atanassov, *J. Power Sources*, 2012, **214**, 303–313.
18 D. G. Lee, O. Gwon, H. S. Park, S. H. Kim, J. Yang, S. K. Kwak, G. Kim and H. K. Song, *Angew. Chem.*, 2015, **127**, 15956–15959.
19 M. Luo, M. Xuan, S. Huo, J. Fan, G. Chakraborty, Y. Wang, H. Zhao, A. Herrmann and L. Zheng, *Angew. Chem., Int. Ed.*, 2020, **59**, 17250–17255.
20 Y. Wang, Z. Chen, Q. Li, X. Wang, W. Xiao, Y. Fu, G. Xu, B. Li, Z. Li, Z. Wu and L. Wang, *Nano Res.*, 2022, DOI: **10.1007/s12274-022-4980-4**.
21 Y. Wang, Q. Sun, Z. Wang, W. Xiao, Y. Fu, T. Ma, Z. Wu and L. Wang, *J. Mater. Chem. A*, 2022, **10**, 16236–16242.
22 W. Yu, Z. Chen, W. Xiao, Y. Chai, B. Dong, Z. Wu and L. Wang, *Inorg. Chem. Front.*, 2022, **9**, 1847–1855.
23 Z. Wang, Y. Wang, W. Xiao, X. Wang, Y. Fu, G. Xu, Z. Li, Z. Wu and L. Wang, *J. Mater. Chem. A*, 2022, **10**, 15155–15160.
24 X. Gao, H. Zhang, Q. Li, X. Yu, Z. Hong, X. Zhang, C. Liang and Z. Lin, *Angew. Chem., Int. Ed.*, 2016, **55**, 6290–6294.
25 X. Gao, G. Li, Y. Xu, Z. Hong, C. Liang and Z. Lin, *Angew. Chem.*, 2015, **127**, 14539–14543.
26 R. W. Grimes, A. B. Anderson and A. H. Heuer, *J. Am. Chem. Soc.*, 1989, **111**, 1–7.
27 C. Guan, X. Liu, W. Ren, X. Li, C. Cheng and J. Wang, *Adv. Energy Mater.*, 2017, **7**, 1602391.
28 A. Rashti, X. Lu, A. Dobson, E. Hassani, F. Feyzbar-Khalkhali-Nejad, K. He and T.-S. Oh, *ACS Appl. Energy Mater.*, 2021, **4**, 1537–1547.
29 Z. Wang, W. Xu, Y. Wang, X. Cui, A. M. Al-Enzi, Y. Tang and G. Zheng, *J. Mater. Chem. A*, 2017, **5**, 7416–7422.
30 X. Chen, L. Luo and Y. Zhang, *Langmuir*, 2021, **37**, 6330–6336.
31 C. Alegre, C. Busacca, A. Di Blasi, O. Di Blasi, A. S. Aricò, V. Antonucci and V. Baglio, *ChemElectroChem*, 2020, **7**, 124–130.
32 M. Prabu, K. Ketpang and S. Shanmugam, *Nanoscale*, 2014, **6**, 3173–3181.
33 X. Liu, Z.-Y. Zhai, Z. Chen, L.-Z. Zhang, X.-F. Zhao, F.-Z. Si and J.-H. Li, *Catalysts*, 2018, **8**, 310.
34 P. Bodhankar, A. Chunduri, N. Patel, D. S. Dhawale, A. Vinu, H. Johani and P. B. Sarawade, *Sustainable Energy Fuels*, 2021, **5**, 1120–1128.
35 P. M. Bodhankar, S. Jadhav and P. B. Sarawade, *Macromol. Symp.*, 2021, **400**, 2100144.
36 P. Giannozzi, S. Baroni, N. Bonini, M. Calandra, R. Car, C. Cavazzoni, D. Ceresoli, G. L. Chiarotti, M. Cococcioni and I. Dabo, *J. Phys.: Condens. Matter*, 2009, **21**, 395502.
37 P. Giannozzi, O. Andreussi, T. Brumme, O. Bunau, M. B. Nardelli, M. Calandra, R. Car, C. Cavazzoni, D. Ceresoli and M. Cococcioni, *J. Phys.: Condens. Matter*, 2017, **29**, 465901.
38 J. Tao, J. P. Perdew, H. Tang and C. Shahi, *J. Chem. Phys.*, 2018, **148**, 074110.
39 S. L. Dudarev, G. A. Botton, S. Y. Savrasov, C. Humphreys and A. P. Sutton, *Phys. Rev. B: Condens. Matter Mater. Phys.*, 1998, **57**, 1505.
40 S. Curtarolo, W. Setyawan, G. L. W. Hart, M. Jahnatek, R. V. Chepulskii, R. H. Taylor, S. Wang, J. Xue, K. Yang, O. Levy, M. J. Mehl, H. T. Stokes, D. O. Demchenko and D. Morgan, *Comput. Mater. Sci.*, 2012, **58**, 218–226.
41 P. Nayak, M. Sahoo and S. K. Nayak, *Ceram. Int.*, 2020, **46**, 3818–3826.
42 Y. K. Mishra, S. Kaps, A. Schuchardt, I. Paulowicz, X. Jin, D. Gedamu, S. Freitag, M. Claus, S. Wille and A. Kovalev, *Part. Part. Syst. Charact.*, 2013, **30**, 775–783.
43 S. K. Meher, P. Justin and G. Ranga Rao, *ACS Appl. Mater. Interfaces*, 2011, **3**, 2063–2073.
44 M.-P. Pileni, *Nat. Mater.*, 2003, **2**, 145–150.
45 T. E. Kibona, *J. Solid State Electrochem.*, 2020, **24**, 1587–1598.
46 Z. Zhu, N. Wei, H. Liu and Z. He, *Adv. Powder Technol.*, 2011, **22**, 422–426.
47 T.-C. Chang, Y.-T. Lu, C.-H. Lee, J. K. Gupta, L. J. Hardwick, C.-C. Hu and H.-Y. T. Chen, *ACS Omega*, 2021, **6**, 9692–9699.
48 E. Umeshbabu, G. Rajeshkhanna, P. Justin and G. R. Rao, *Mater. Chem. Phys.*, 2015, **165**, 235–244.
49 B. Wang, C.-W. Tsang, K. H. Li, Y. Tang, Y. Mao and X.-Y. Lu, *Nanoscale Res. Lett.*, 2019, **14**, 6.
50 L. Yang, B. Zhang, B. Fang and L. Feng, *Chem. Commun.*, 2018, **54**, 13151–13154.
51 L. Zhang, Y. Li, J. Peng and K. Peng, *Electrochim. Acta*, 2019, **318**, 762–769.
52 M. Cheng, H. Fan, Y. Song, Y. Cui and R. Wang, *Dalton Trans.*, 2017, **46**, 9201–9209.
53 L. Fang, Z. Jiang, H. Xu, L. Liu, X. Gu and Y. Wang, *J. Catal.*, 2018, **357**, 238–246.
54 H.-Y. Wang, Y.-Y. Hsu, R. Chen, T.-S. Chan, H. M. Chen and B. Liu, *Adv. Energy Mater.*, 2015, **5**, 1500091.
55 S. Sun, H. Li and Z. J. Xu, *Joule*, 2018, **2**, 1024–1027.
56 P. Acharya, J. Burrow, M. Abolhassani and L. F. Greenlee, *ECS Trans.*, 2018, **85**, 81.
57 J. Chen, X. Wu and A. Selloni, *Phys. Rev. B*, 2011, **83**, 245204.
58 S.-F. Hung, C.-W. Tung, T.-S. Chan and H. M. Chen, *CrystEngComm*, 2016, **18**, 6008–6012.
59 C. C. McCrory, S. Jung, J. C. Peters and T. F. Jaramillo, *J. Am. Chem. Soc.*, 2013, **135**, 16977–16987.
60 H. Wang, Q. Gao and L. Jiang, *Small*, 2011, **7**, 2454–2459.
61 Q. Liu, X. Zhang, B. Yang, J. Liu, R. Li, H. Zhang, L. Liu and J. Wang, *J. Electrochem. Soc.*, 2015, **162**, E319.

62 C. Zhu, S. Fu, D. Du and Y. Lin, *Chem.–Eur. J.*, 2016, **22**, 4000–4007.
63 J. Haenen, W. Visscher and E. Barendrecht, *J. Electroanal. Chem. Interfacial Electrochem.*, 1986, **208**, 273–296.
64 N.-U.-A. Babar and K. S. Joya, *ACS Omega*, 2020, **5**(19), 10641–10650.
65 S. Anantharaj, S. Ede, K. Karthick, S. S. Sankar, K. Sangeetha, P. Karthik and S. Kundu, *Energy Environ. Sci.*, 2018, **11**, 744–771.
66 J. Song, C. Wei, Z.-F. Huang, C. Liu, L. Zeng, X. Wang and Z. J. Xu, *Chem. Soc. Rev.*, 2020, **49**, 2196–2214.
67 I. Heller, J. Kong, K. A. Williams, C. Dekker and S. G. Lemay, *J. Am. Chem. Soc.*, 2006, **128**, 7353–7359.
68 S. Adhikari, Y. Kwon and D.-H. Kim, *Chem. Eng. J.*, 2020, **402**, 126192.
69 R. Vadakkekara, R. Illathvalappil and S. Kurungot, *ChemElectroChem*, 2018, **5**, 4000–4007.
70 M. Yang, W. Lu, R. Jin, X.-C. Liu, S. Song and Y. Xing, *ACS Sustainable Chem. Eng.*, 2019, **7**, 12214–12221.
71 L. Yang, L. Chen, D. Yang, X. Yu, H. Xue and L. Feng, *J. Power Sources*, 2018, **392**, 23–32.
72 E. Umeshbabu, P. Hari Krishna Charan, P. Justin and G. Ranga Rao, *ChemPlusChem*, 2020, **85**, 183–194.
73 S. M. N. Jeghan and G. Lee, *Nanotechnology*, 2020, **31**, 295405.
74 X. Xiao, X. Hu, Y. Liang, G. Zhang, X. Wang, Y. Yan, X. Li, G. Yan and J. Wang, *J. Power Sources*, 2020, **476**, 228684.

